US Department of Energy, Office of Energy Efficiency & Renewable Energy

Low Impedance Cathode/Electrolyte Interfaces for High Energy Density Solid-State Batteries

Project Period: October 1, 2019 – May 31, 2023

PI: Eric D. Wachsman, Ph.D.
Director, Maryland Energy Innovation Institute
William L. Crentz Centennial Chair in Energy Research
University of Maryland
College Park, MD 20742
ewach@umd.edu
Tel.: (301) 405-8193, Fax.: (301) 314-8514

Co-PI: Yifei Mo, PhD.
University of Maryland College Park
University of Maryland
College Park, MD 20742
E-mail: yfmo@umd.edu

Submission Date: August 31, 2023

Award No. DEEE0008858

Stephanie Swann
Digitally signed by Stephanie Swann
DN: cn=Stephanie Swann, o=University of Maryland, ou=VPR-Office of Research Administration, email=smbrack@umd.edu, c=US
Date: 2023.09.07 17:00:19 -04'00'

Submitting Official: Stephanie M. Swann
Assistant Director
Office of Research Administration
Room 3112 Lee Building, 7809 Regents Drive, College Park, MD, 20742
Email: smbrack@umd.edu,
Phone (301) 405-8079

TABLE OF CONTENTS

Low Impedance Cathode/Electrolyte Interfaces for High Energy Density Solid-State Batteries

Project Introduction

All-solid-state batteries (ASSBs) using a ceramic fast Li-ion conductor as a solid-state electrolyte (SSE) have been proposed as a promising strategy to significantly increase the energy density of lithium batteries. Due to their high ion conductivity and excellent stability, Li-stuffed garnets exhibit the most promising physical and chemical properties for SSEs. However, the typical microstructure, thick (>100 μm) bulk electrolyte and simple planar electrode/electrolyte interfaces, combined with poor electrode wetting of the garnet result in excessively high area specific resistances (ASRs) that severely limit achievable current density and cell energy density.

Recently, the University of Maryland PIs have pioneered thin garnet-based solid-state batteries that effectively address the interfacial impedance at the Li metal side. We have demonstrated the ability to overcome the solid-electrolyte/solid-electrode interfacial impedance using interfacial engineering [1] of solid-state garnet (e.g. $Li_7La_3Zr_2O_{12}$ LLZ) electrolytes under BMR contract DEEE0006860. Further, we have demonstrated Li-metal anodes with unique porous-dense-porous trilayer LLZ architectures achieving excellent stability and high current density (10 mA/cm^2) for Li-cycling with no electrical shorting [2] successfully solving the high Li-garnet interfacial impedance that severely limited achievable current density. We have also developed state-of-the-art Li-metal solid-state batteries using this technology demonstrating high energy density (~300Wh/kg) with both NMC high-voltage [3] and S high-capacity [4] cathodes using these trilayer garnet structures.

However, cycling rate in full cells is orders of magnitude lower than Li-symmetric cells as issues remain with regard to properties evolving at the cathode-electrolyte interface. Today's processing routes require temperatures of ≥1000°C for the garnet, which unavoidably leads to enhanced ion diffusion at the interface, thereby raising the issues of material compatibility and the formation of possible interphases that influence the total cell resistance for desired cathode/electrolyte co-sintering. In addition, even with cathodes infiltrated into pre-sintered garnet structures major challenges still exist at the cathode interfaces for all-solid-state batteries, including (1) high cathode interfacial resistance and (2) limited processing techniques that incorporate active cathode materials within the solid electrolyte.

Objectives

The project objective is to integrate computational and experimental research to develop and test Li-metal-based batteries that implement solid SSEs equipped with NMC cathodes integrated into the Li-metal/LLZ tri-layer architecture. Specifically, the team is achieving the following: (1) identify and demonstrate interfacial layers to achieve low-impedance and stable NMC/LLZ interfaces; (2) develop novel processing techniques to fabricate NMC/LLZ composite cathodes with low interfacial resistance; and (3) enable high-performance ASSBs with an energy density of 450 Wh/kg and 1400 Wh/L and negligible degradation for 500 cycles.

Approach

In this new project, the team is building on their demonstrated expertise with garnet electrolytes and ASSBs to accomplish the following: (1) engineer interfaces to overcome high NMC/LLZ interfacial impedance and interfacial degradation; (2) develop processing and fabrication techniques to achieve high-loading NMC/LLZ composite cathodes with low resistance and high cyclability; and (3) integrate the NMC/LLZ cathodes into all-solid-state Li-metal/LLZ cells to achieve high-energy-density batteries.

Results

COVID-19 Impact- Progress on experimental results were impacted by COVID19 which closed labs for several months resulting in a 6 month no-cost extension.

Thermochemical stability between LLZ and NMC

The reactivity of $LiNi_xMn_yCo_zO_2$ (x+y+z=1) (NMC) with $Li_{6.75}La_3Zr_{1.75}Ta_{0.25}O_{12}$ (LLZTO) was investigated by DSC of the powder mixture. All NMCs show an endothermic peak at 700°C (Figure *1*), corresponding to a kinetically slow reaction with garnet. Most notably, the scan for NMC811 shows a baseline that continues to increase after 700°C until another large endothermic peak beginning at 900°C emerges. This reaction above 900°C matches the XRD results indicating there is a strong reaction between NMC811 and LLZTO. Additionally, this large endothermic peak is similarly observable in the NMC622 and NMC532 samples but has a higher onset temperature with decreasing Ni content. This feature is not observable in the measured temperature range for lower Ni content NMCs. These results support the computational trend (below) that NMC and LLZTO react more strongly with increasing Ni content.

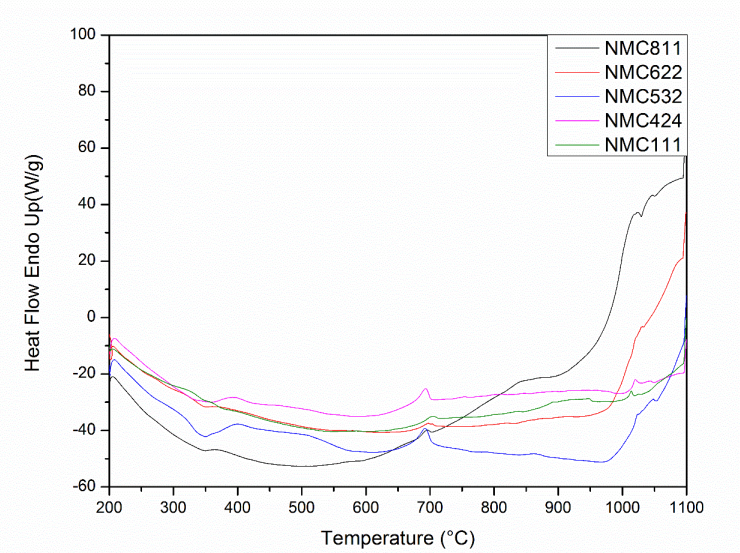

Figure 1. DSC curves of 50/50 w/w mixtures of LLZTO with NMCs of various compositions.

To investigate the effect of lithium content on the high temperature stability of NMC against LLZTO, LLZTO was synthesized with 10% and 40% molar excess Li and mixed with NMC111, heated at various temperatures in air, and then characterized by XRD and DSC. No new phases were detected by XRD in the mixtures with 40mol% excess Li even after sintering to 900 °C (Figure 2a), indicating the reaction between the two materials with 10mol% excess Li was mainly caused by Li deficiency at high temperature. In the DSC curve (Figure 2b), the endothermic peak detected at 700°C for the mixture with 10% excess Li LLZTO is missing for the mixture with 40% excess Li LLZTO, indicating the endotherm reaction is related to the loss of Li at high temperature.

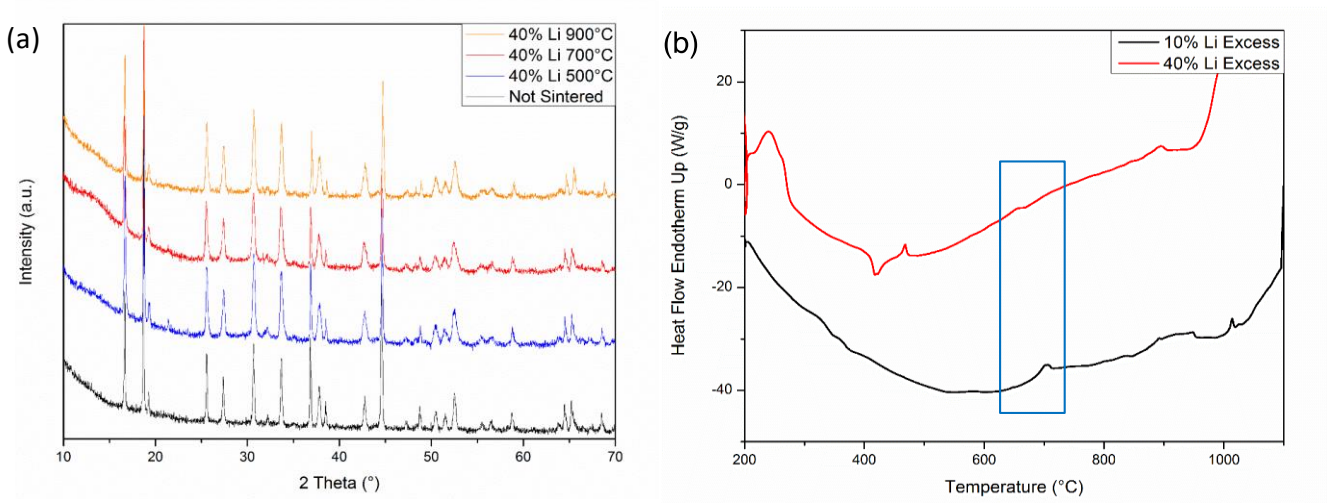

Figure 2. (a) XRD and (b) DSC curves of 50/50 w/w mixtures of LLZTO (with 10mol% or 40 mol% excess Li) with NMC-111.

Computations of promising coating materials to stabilize the LLZ-NMC Interface

Using demonstrated thermodynamic analyses for interface stability based on first-principles computation, we studied the trends in stability with LLZO and NMC throughout the entire Li-M-O ternary composition space, in order to identify all compositions that are stable with LLZO as promising coating. The decomposition energy E_d of each composition with LLZO is illustrated by a heatmap of Li-M-O Gibbs ternary diagram (Figure 3). Li-M-O systems with different cations M exhibit significantly different stability with LLZO. We extended our analysis to other Li-M-O systems for cations M = B, C, N, Al, Si, P, Ti, V, Cr, Zr, Nb, Mo, Zn, Ga, Ge, Ta, or W, which are commonly considered and used for coatings (Figure 3). Many systems with nonmetal M such as B, Al, Si, P only have one or two ternary Li-M-O compositions (in addition to Li_2O and Li_2O_2) stable with LLZO, leading to a narrow compositional space with good LLZO stability. The transition metal elements V, Cr, Nb, Ta, Zn, Ga, Ge and nonmetals C and N are stable with garnet, and a wider Li-M-O compositional space of ternary Li-M-O oxides have good stability with LLZO. For cations M = Ti and Zr, the M metal exhibits minor reactions with LLZO, but the binary oxides M-O are stable with LLZO, leading to a wide compositional space stable with LLZO. Notably, for the Li-Zn-O system, Zn metal, ZnO oxide, and LiZn alloy are stable with LLZO. Thus, this system has the widest composition space stable with LLZO, and so should be a promising system for garnet coatings as has been demonstrated in experiments. In general, one shall select within this stable compositional space for garnet coatings, as the compositions outside react exothermically with LLZO and may cause side reactions and interfacial degradation. Our Li-M-O heatmaps of the stability with LLZO provide guiding maps for selecting compositions for garnet coating layers.

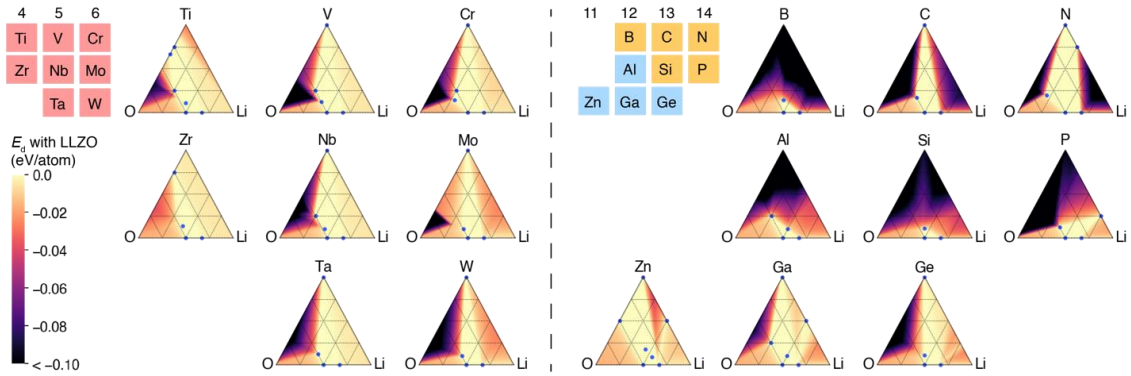

Figure 3. Heatmaps of chemical stability (Ed) of Li-M-O (M = B, C, N, Al, Si, P, Ti, V, Cr, Zr, Nb, Mo, Zn, Ga, Ge, Ta, or W) with LLZO. Known compounds that are stable with LLZO are marked with blue points.

In addition, we also analyzed the stability of the entire Li-M-O composition space with NMC (Figure 4). Our analyses found that the only Li-M-O compositions stable with the cathode are along the tie-line of Li_2O and M-O metal oxides, and the cathode stability is generally good for O-rich compositions. We identify the coating layer stable with both SE and cathode, by combining the heatmaps and stable regions of Li-M-O with LLZO and those with NMC cathode. The materials compositions along the tie-line of Li_2O to M-O oxides, including multiple ternary oxides, show decent stability with both LLZO and NMC. In summary, we have successfully achieved our milestone of identifying promising coating materials determine appropriate compositions to stabilize the LLZO-NMC interface.

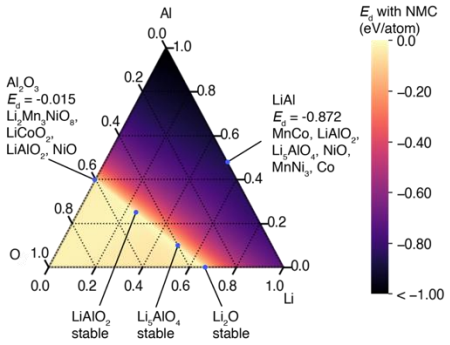

Figure 4. Heatmap of the decomposition energy of Li-Al-O compositions with NMC 111.

Thermochemical stability between LLZ and infiltrated NMC and the effect of interfacial coating layers

Co-sintering of garnet trilayer structures with NMC622 filling into the porous layers was carried out at 500°C, 700°C, and 800°C for 3hrs on both uncoated and atomic layer deposition (ALD) coated structures under Ar atmosphere. Al_2O_3 and ZnO were used as the coating layer. These samples were then assembled into symmetric cells and EIS was performed to observe the effect of the ALD layer on the impedance of these cells. As shown by the EIS Nyquist plots and Distribution of Relaxation Times (DRT) analysis in Figure 5, Al_2O_3 coating can significantly reduce the overall interfacial impedance at above 700°C. Whereas, ZnO coating can only reduce the overall interfacial impedance at 700°C but essentially had no effect at 800°C (Figure 6). These results indicate that Al_2O_3 is better than ZnO at improving the interfacial impedance.

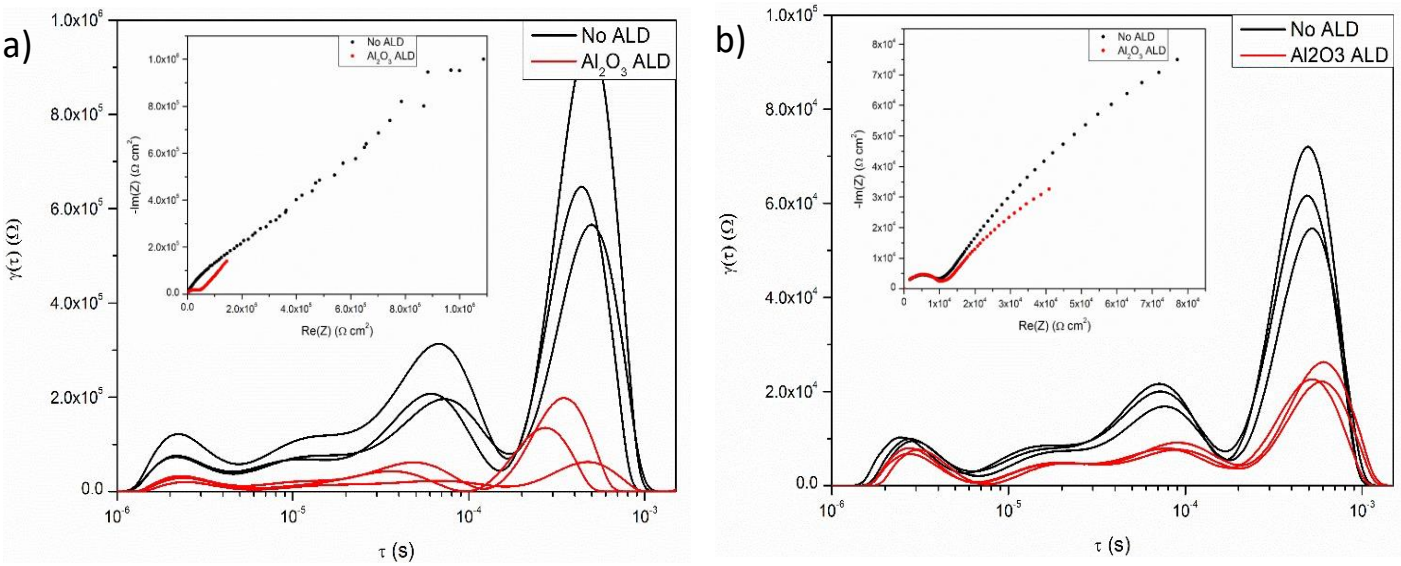

Figure 5 Nyquist plot (inset) and DRT Analysis for symmetric NMC622|LLZO|NMC622 cells with and without Al_2O_3 coating co-sintered at (a) 700°C and (b) 800°C.

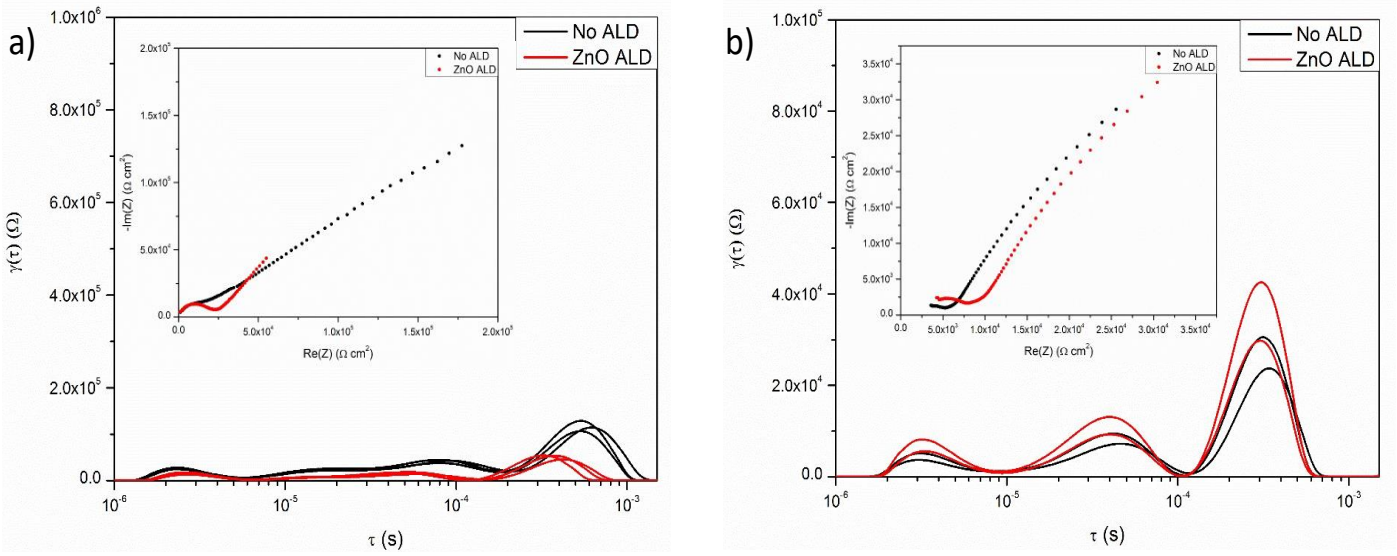

Figure 6 Nyquist plot (inset) and DRT Analysis for symmetric NMC622|LLZO|NMC622 cells with and without ZnO coating co-sintered at (a) 700°C and (b) 800°C.

To determine the effect of the interlayer thickness on its ability to improve the interfacial impedance of NMC symmetric cells, samples were coated with different thicknesses of ALD alumina and co-sintered at 800°C. Figure 7 demonstrates that the 3nm (15 cycles of ALD) interlayer has a 4x reduction in the ASR, whereas the 6nm (30 cycles) interlayer appears to have similar ASR to the uncoated samples.

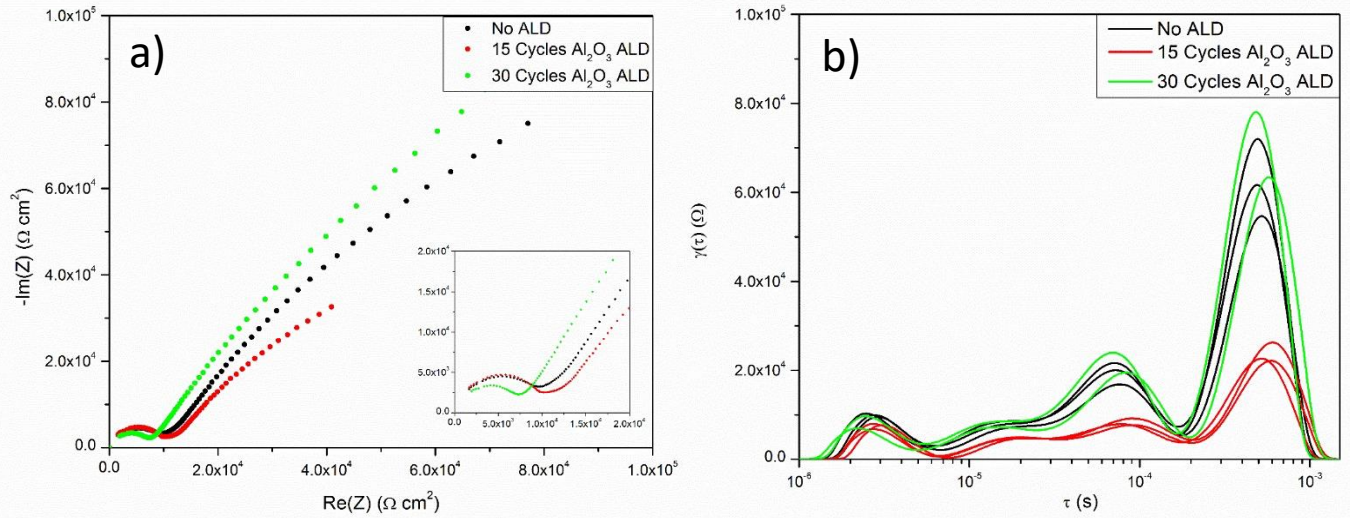

Figure 7 a) Nyquist plot and b) DRT plot for symmetric NMC622|LLZO|NMC622 cells co-sintered at 800°C comparing uncoated and Al_2O_3 ALD coated samples.

Due to the computational and DSC results indicating that adding additional Li would prevent the reaction of NMC and LLZTO, symmetric NMC cells were co-sintered at 800°C with additional lithium from either LiOH or Li_2CO_3 as the source in a molar ratio of 1:3 (Li:NMC). Figure 8 shows the EIS results for these experiments, demonstrating a more than 10X reduction of the ASR, regardless of Li source. This achieves the 10X ASR reduction milestone and confirms the predicted results that increasing the amount of available Li would reduce the reaction of NMC and LLZTO. Furthermore, this reduction can be integrated with the ALD interlayers for even greater reduction in interfacial impedance (Figure 9). Given the results showing that the

6nm interlayer had higher ASR than the 3nm interlayer, this suggests that the thicker interlayer was not sufficiently lithiated since the ionic conductivity of lithiated alumina is several orders of magnitude higher than that of unlithiated alumina.

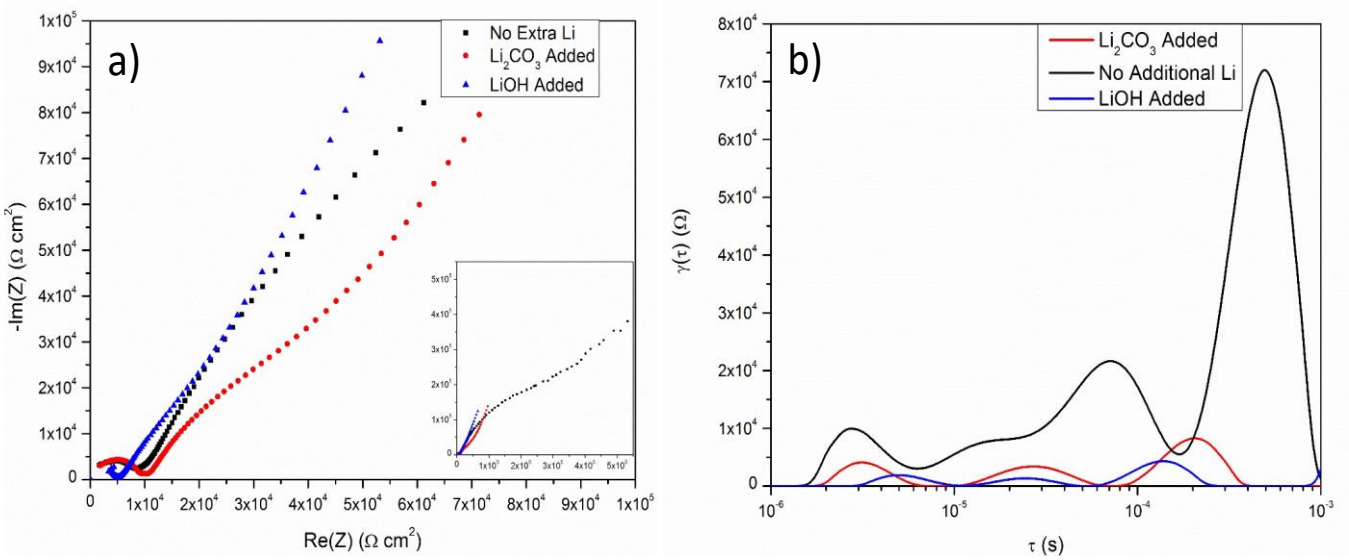

Figure 8 a) Nyquist plot and b) DRT plot for symmetric NMC622|LLZO|NMC622 cells co-sintered at 800°C comparing samples with and without extra Li from various sources.

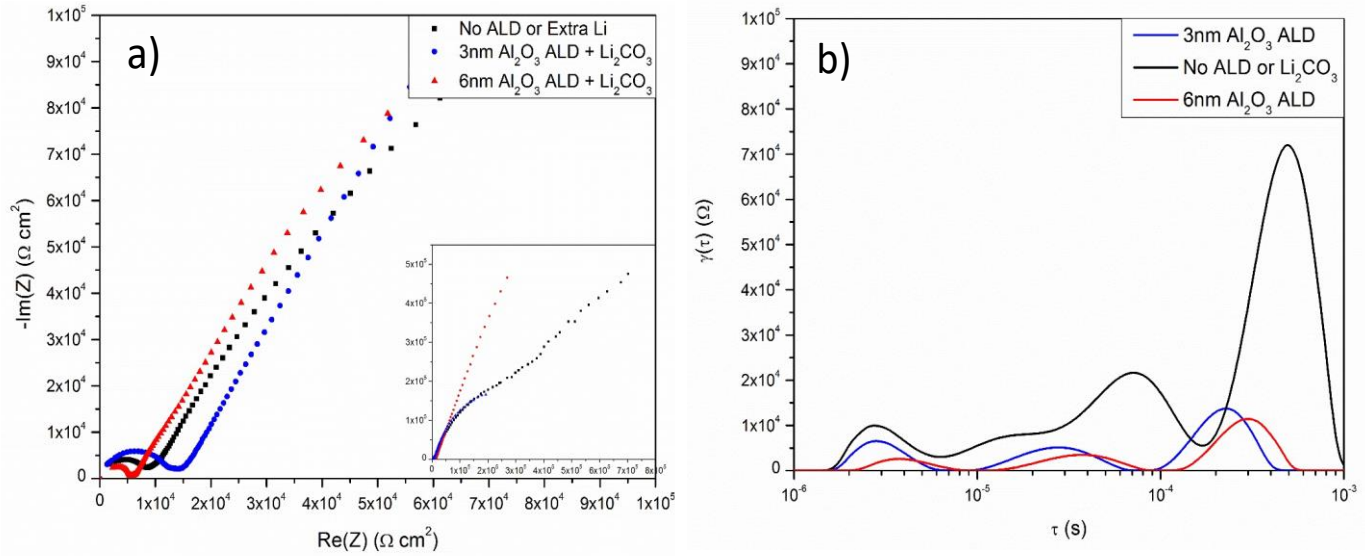

Figure 9 a) Nyquist plot and b) DRT plot for symmetric NMC622|LLZO|NMC622 cells co-sintered at 800°C comparing various thicknesses of Al_2O_3 coated samples, all with the same amount of extra Li added.

The amount of extra Li was increased to get a sense for how much additional Li is beneficial to NMC/LLZTO co-sintering. The Li:NMC ratio was increased to 1:1. The Nyquist and DRT plots (Figure 10) show that both ratios significantly decrease the ASR when compared to samples without extra Li.

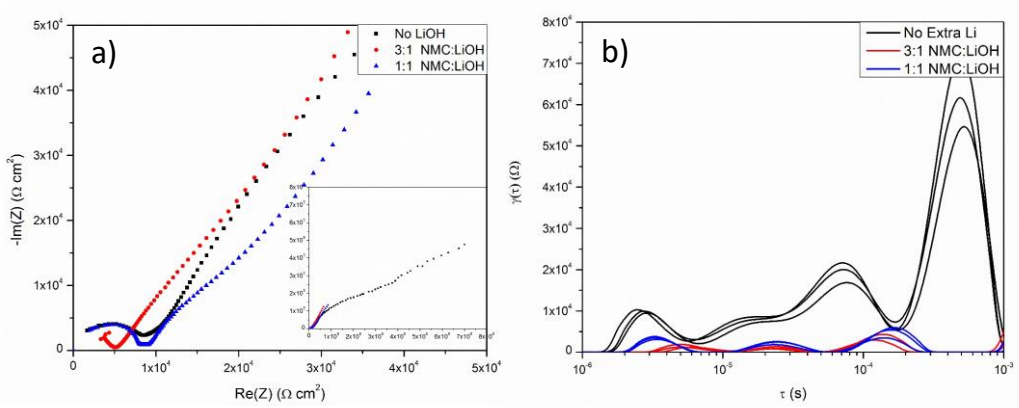

Figure 10 a) Nyquist plot and b) DRT plot for symmetric NMC622|LLZO|NMC622 cells co-sintered at 800°C comparing samples where the extra Li ratio was increased from 1:3 Li:NMC to 1:1.

Thermochemical stability between LLZ and interface coated NMC (Experimentally determined)

XRD results of sintered NMC/$Li_{6.75}La_3Zr_{1.75}Ta_{0.25}O_{12}$ (LLZTO) pellets suggested that NMCs with higher Ni contents (e.g., NMC811) are more reactive towards garnet than those with lower amounts of Ni. NMC811/LLZTO pellets demonstrated near complete loss of peak intensity in XRD when sintered at 1000°C. To further investigate this effect, TGA/DSC was performed on samples of the pristine NMCs in both Ar and O_2 atmosphere as literature reports indicate NMC loses O_2 from the lattice at high temperatures. The TGA results are shown in Figure 11 and show that the higher the Ni content of NMC, the greater the mass loss with an earlier onset temperature. Furthermore, the samples heated in an O_2 environment show decreased mass loss with an increase in the onset temperature across all compositions of NMC. This stabilization of the NMC is significant enough that NMC111 demonstrates nearly no mass loss up to 1100°C in O_2. Additionally, coating NMC622 with a 4nm layer of alumina further reduces the mass loss of NMC622, such that in O_2 atmosphere the sample loses less than 0.5wt%. This suggests that careful selection of co-sintering environment, use of a protective ALD coating, as well as the NMC composition should be done when co-sintering NMC and LLZTO.

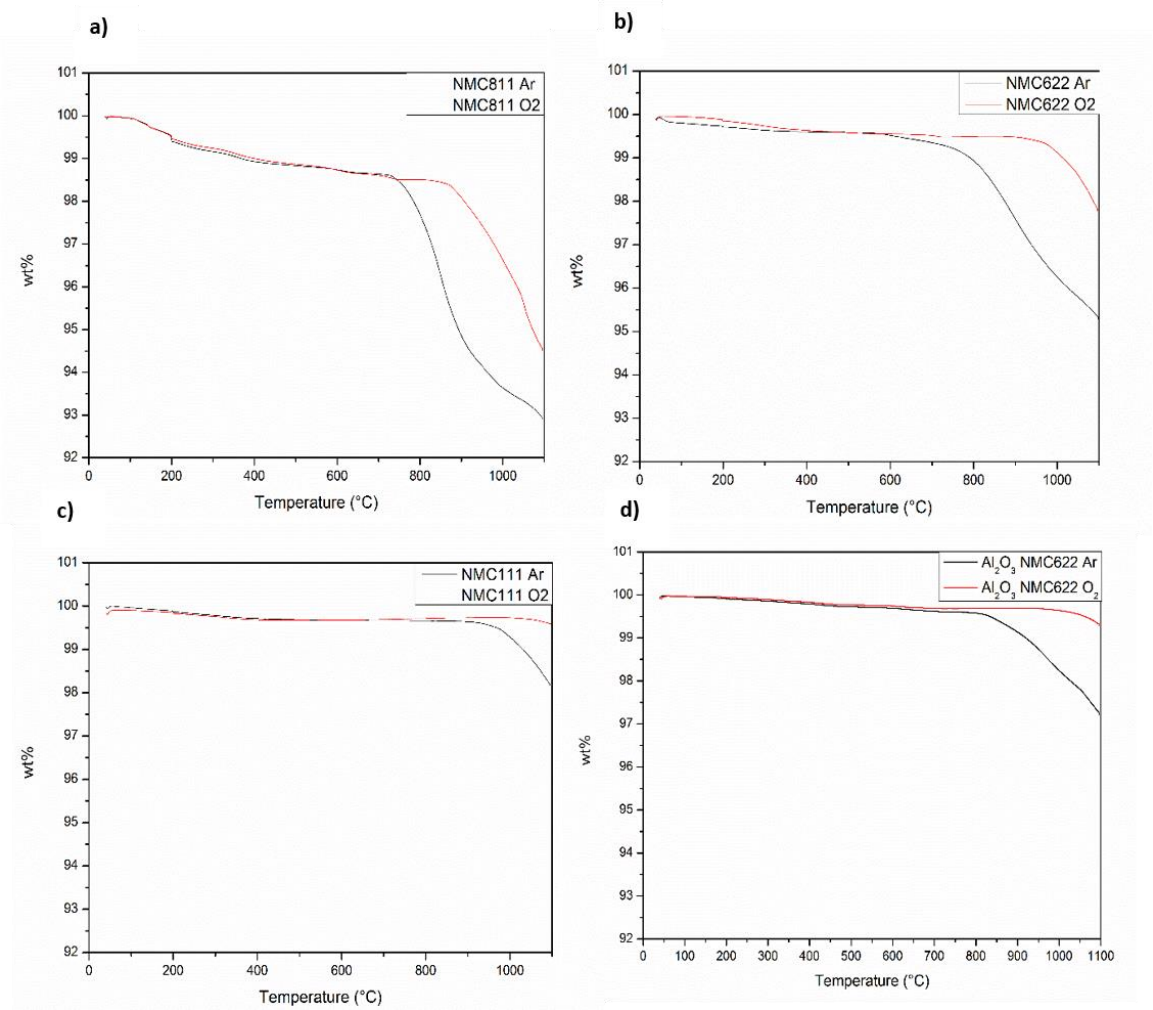

Figure 11. TGA results of a) NMC811, b) NMC622, c) NMC111, and d) Al2O3 coated NMC622 in both Ar and O_2 atmospheres.

Figure 12 contains the summarized phase weight percentage results of the Rietveld Refinement of the powder XRD spectra. The samples consisted of NMC and LLZTO in a 1:1 weight ratio co-sintered at 900°C for 3hrs in Ar and O_2. The results for samples co-sintered in air are not included as they show similar results to those processed in O_2 except that the weight percent of NMC is slightly lower indicating and intermediate

thermochemical stability between Ar and O_2 of NMC. Across all NMC compositions, the wt% of NMC decreases with increasing Li content of the LLZO, indicating either a loss of NMC crystallinity or formation of amorphous decomposition phases. For higher Ni content NMCs, the increase in Li content is also correlated with an increase in the formation of a perovskite-like decomposition phase, $La_2Li_{0.5}M_{0.5}O_4$ (M=Ni, Mn, Co). It is unclear what the exact composition of the transition metal site is because all these compositions have very similar XRD patterns. Furthermore, more perovskite is formed when NMC811 is co-sintered than NMC622. This combined with the TGA/DSC results seems to indicate that the lower the thermochemical stability of the pure NMC and higher Li content in the LLZO leads to greater formation of the perovskite decomposition phase (NMC811 demonstrated greater O_2 mass loss starting at lower temperatures than NMC622). This trend holds true regardless of the co-sintering atmosphere.

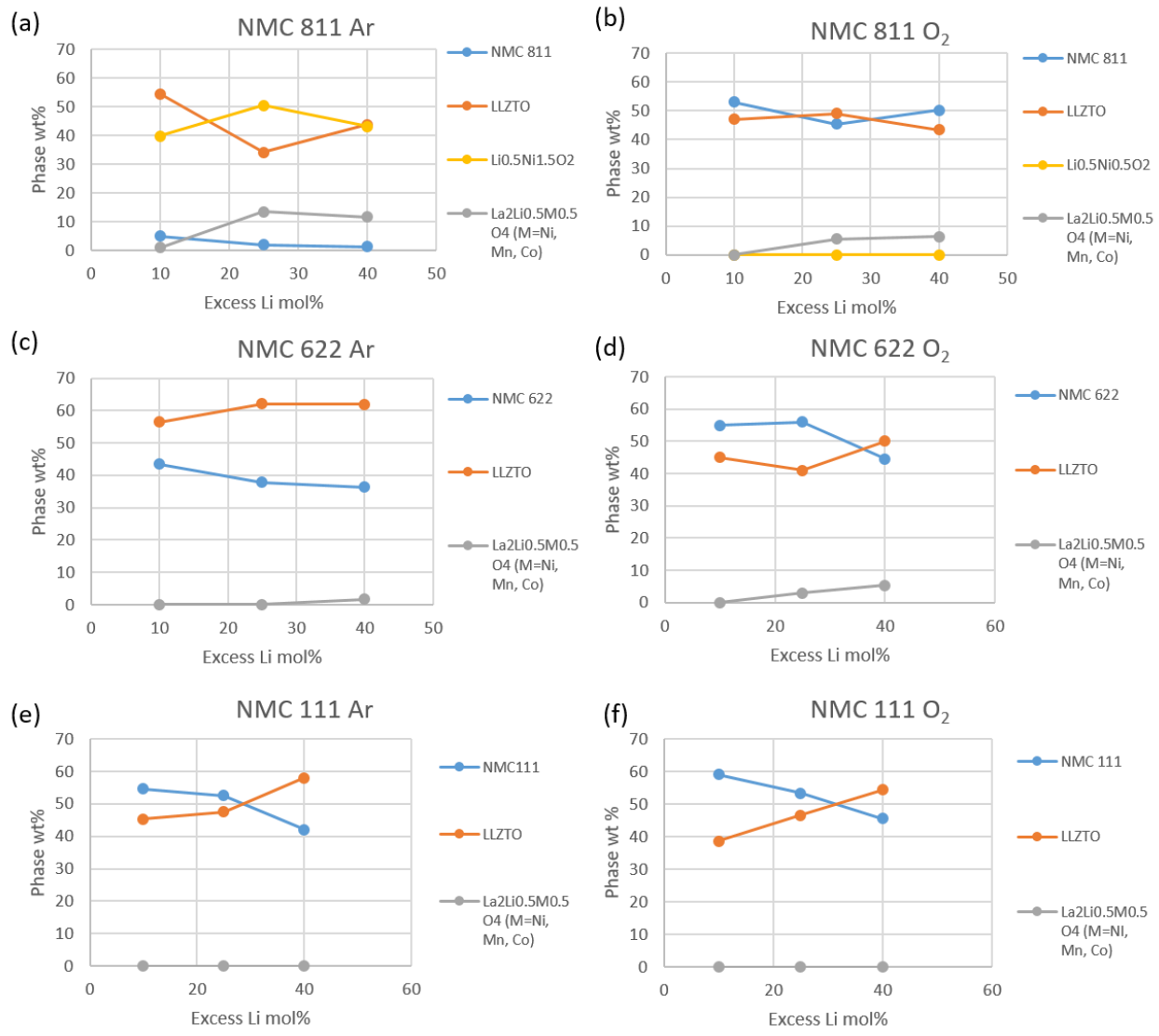

Figure 12. XRD and Rietveld Refinement Analysis of a-b) NMC811, c-d) NMC622, and e-f) NMC111 co-sintered in a 1:1 wt ratio with LLZTO of varying amounts of excess Li in both Ar and O_2 atmospheres

Across all NMC compositions, the wt% of NMC is lower for samples sintered in Ar than those sintered in O_2. This reinforces the importance of having high oxygen partial pressure to prevent O_2 loss from the NMC that leads to subsequent decomposition. This difference is smaller for NMC111 and becomes greater for NMC622 and greatest for NMC811. It is notable that for NMC811 co-sintered in Ar, less than 10wt% is still the NMC

phase, as a high Ni-content lithiated spinel phase ($Li_{0.5}Ni_{1.5}O_2$) is detected instead. In O_2, the NMC811 phase is largely preserved. Additionally, the weight fraction of the perovskite decomposition phase is higher for NMC811 co-sintered in Ar than in O_2. This suggests that stabilizing the NMC is of the utmost importance to prevent formation of decomposition products like $La_2Li_{0.5}M_{0.5}O_4$ (M=Ni, Mn, Co).

Various coatings of lithium silicates and lithium aluminates with varying lithium content and at varying sintering atmosphere was studied. Thin layers of lithium silicates and aluminates were coated over NMC622 through solution-based synthesis route. (Please note in the following experiments we have used NMC622 for the studies). Figure 13 shows the summarized phase weight percentage results of the Rietveld Refinement of the powder XRD spectra of LLZTO and lithium silicate coated NMC622. Two species of lithium silicate was used: Li_2SiO_3 and lithium rich Li_4SiO_4. With 40mol% excess Li, for uncoated NMC sample about 2 wt% of perovskites were formed. In addition, with the silicate coated sample, NMC phase % was higher when sintered in O_2 atmosphere (45%) compared to the uncoated sample (35%). Further, when the samples were sintered in Ar atmosphere $La_2Li_{0.5}M_{0.5}O_4$ (M=Ni, Mn, Co) phase increases with increasing Li content.

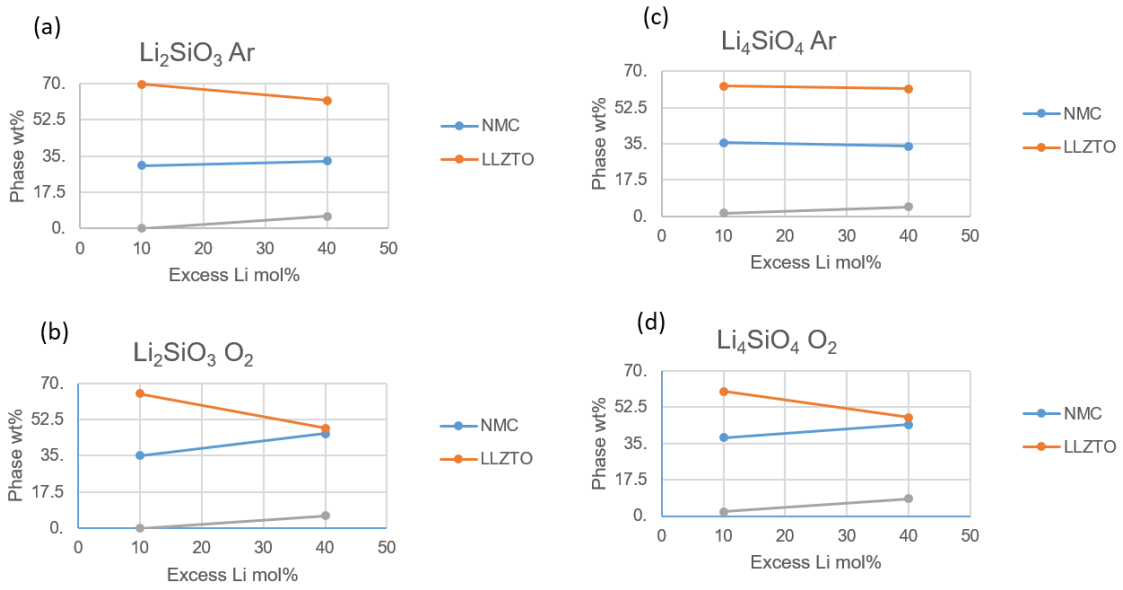

Figure 13. Rietveld Refinement Results of XRD of Li_2SiO_3-NMC622 co-sintered in a 1:1 wt ratio with LLZTO onto LLZTO trilayers at 900°C in (a) Ar atmosphere and (b) O2 atmosphere. Similarly, Rietveld refinement results of XRD of Li_4SiO_4-NMC622 sintered in (c) Ar and (d) O2 atmosphere.

Figure 14 shows the Rietveld refinement analysis of lithium aluminate coated NMC with garnet solid electrolyte sintered at different sintering atmosphere (Ar and O_2). When sintered in Ar atmosphere, the phase wt% of NMC is unchanged and the presence of coating phase decreased the formation of $La_2Li_{0.5}M_{0.5}O_4$ (M=Ni,Mn,Co) decomposition phase.

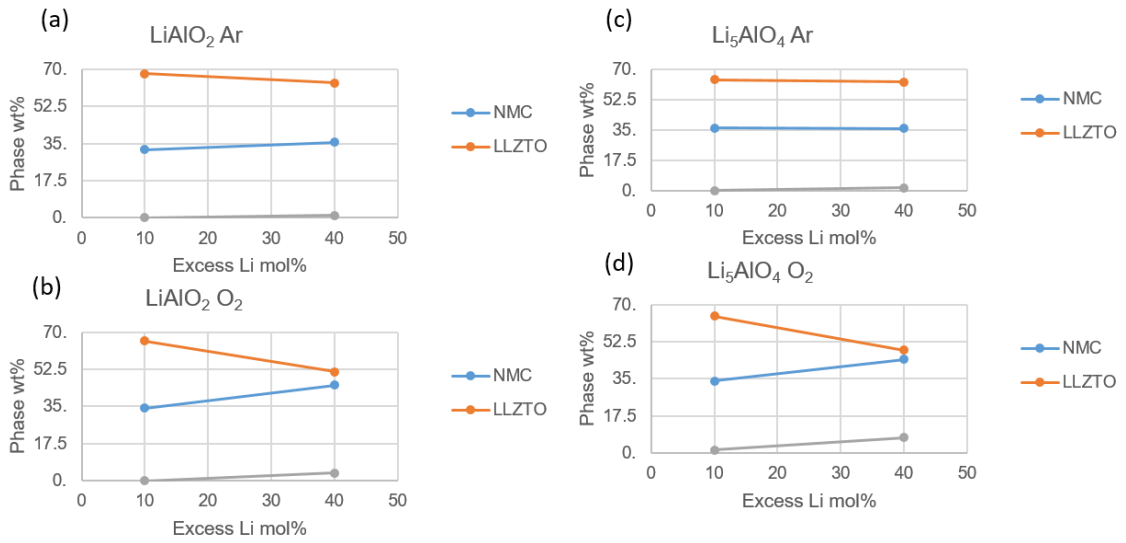

Figure 14. Rietveld Refinement Results of XRD of $LiAlO_2$-NMC622 co-sintered in a 1:1 wt ratio with LLZTO onto LLZTO trilayers at 900°C in (a) Ar atmosphere and (b) O_2 atmosphere. Similarly, rietveld refinement results of XRD of Li_5AlO_4-NMC622 sintered in (c) Ar and (d) O_2 atmosphere.

Computational results and model refined for process optimization

The computation model results for interface side reactions were compared with experimental results. The experimental results reported the formation of delithiated phases as side products in agreement with our computation predictions. For the process optimization, experimental results shown improvement in interface stability using oxygen gas environment. To improve our model to account for the process optimization, we include the sintering environment into our computation model using the grand potential phase diagram approach. In the improved model, the external environment is open to the interface for the potential reaction evaluations. Our models consider the environment in two ways. One way is through the control of Li chemical potential (Table 1), which is a key element loss during sintering, and can be strongly interacting with the environment. Thus, the environment chemical potential can be translated into the Li chemical potential. In our results, we observe having an appropriate range of Li chemical potential can reduce Li loss and also promote the formation of passivation layer such as Li_2O, which can kinetically limit Li loss and mitigate the side reaction (Table 1). In another model, we directly consider the oxygen gaseous environment (Table 2). In this model, we observe significant stabilization of the cathode materials (Table 2), in agreement with the reported experimental results. In summary, computation models for process optimization were developed achieving good agreement with experiment. In addition, as shown above, the experimental results for inter-layer materials are compared with computation results. The coating layer materials predicted by computation are now verified by experiments. These coating layers show good stabilities and good conductive properties, confirming and verifying the computation prediction of the stable coating between garnet and cathode.

Table 1. Stability of LLZO–NMC 111 Under Varying Li Chemical Potential.

μ_{Li} (eV)	ratio of NMC	ratio of LLZO	Mutual Rxn. E. (meV/atom)	Phase equilibria
0	0.43	0.57	-81	La_2O_3, Li_2O, $ZrCo_2$, $ZrMn_2$, $ZrNi_3$
-0.25	0.75	0.25	-29	La_2O_3, Li_2O, MnCo, Zr_6Co_{23}, $ZrNi_3$
-0.5	1.00	0.00	0.00	Co, Li_2O, MnCo, $MnNi_3$
-1	0.53	0.47	-27	Co, La_2MnCoO_6, Li_2O, $Li_6Zr_2O_7$, $MnNi_3$
-1.25	0.43	0.57	-87	Co, La_2MnCoO_6, Li_2O, $Li_6Zr_2O_7$, Ni
-1.75	0.43	0.57	-155	La_2MnCoO_6, Li_2O, Li_6CoO_4, $Li_6Zr_2O_7$, Ni
-2	0.43	0.57	-151	La_2MnCoO_6, Li_2O, $Li_6Zr_2O_7$, $LiCoO_2$, Ni
-2.25	0.43	0.57	-139	La_2MnCoO_6, Li_2O, $Li_6Zr_2O_7$, $LiCoO_2$, NiO
-2.75	0.43	0.57	-125	La_2MnCoO_6, Li, Li_2NiO_3, Li_2O, $Li_6Zr_2O_7$, $LiCoO_2$
-3	0.43	0.57	-138	La_2MnCoO_6, Li, Li_2NiO_3, Li_2O_2, $Li_6Zr_2O_7$, $LiCoO_2$
-3.25	0.43	0.57	-146	La_2MnCoO_6, Li, Li_2NiO_3, Li_2O_2, Li_2ZrO_3, $LiCoO_2$
-3.5	0.43	0.57	-140	La_2MnCoO_6, Li, Li_2NiO_3, $LiCoO_2$, O_2, ZrO_2
-3.75	0.43	0.57	-158	La_2MnCoO_6, Li, $Li(CoO_2)_2$, NiO, O_2, ZrO_2
-4	0.43	0.57	-168	CoO_2, La_2MnCoO_6, Li, NiO, O_2, ZrO_2

Table 2. Stability of LLZO–NMC 111 Interface Under Varying O_2 Chemical Potential

μ_O (eV)	ratio of NMC	ratio of LLZO	Mutual Rxn. E. (meV/atom)	Phase equilibria
0.00	0.43	0.57	-141	La_2MnCoO_6, Li, Li_2NiO_3, Li_2O_2, $Li_6Zr_2O_7$, $LiCoO_2$
-0.25	0.43	0.57	-145	La_2MnCoO_6, Li, Li_2NiO_3, Li_2O_2, Li_2ZrO_3, $LiCoO_2$
-0.50	0.43	0.57	-141	La_2MnCoO_6, Li, Li_2NiO_3, $LiCoO_2$, O_2, ZrO_2
-0.75	0.43	0.57	-160	La_2MnCoO_6, Li, $Li(CoO_2)_2$, NiO, O_2, ZrO_2
-1.00	0.43	0.57	-168	CoO_2, La_2MnCoO_6, Li, NiO, O_2, ZrO_2

Demonstrating 10X reduction in interfacial resistance between coated and uncoated LLZTO/NMC interfaces

Various interlayer coatings identified by the computational work were synthesized on the surface of NMC622 via a solution-based process. These include $LiAlO_2$, Li_2SiO_3, and Li_2ZrO_3. These coated NMC powders were then co-sintered in a 1:1 weight ratio of NMC: LLZTO at 1000°C in O_2 onto LLZTO trilayers to fabricate symmetric cells for EIS testing. These results for varying coating thicknesses are summarized in Figure 15. Shown in Figure 15a-b, 2.5mol% was the optimal coating thickness for the Li_2ZrO_3 leading to a 2.5X reduction in the impedance. For the $LiAlO_2$ and Li_2SiO_3 coatings, 10mol% was optimal both leading to a 4X reduction in the impedance.

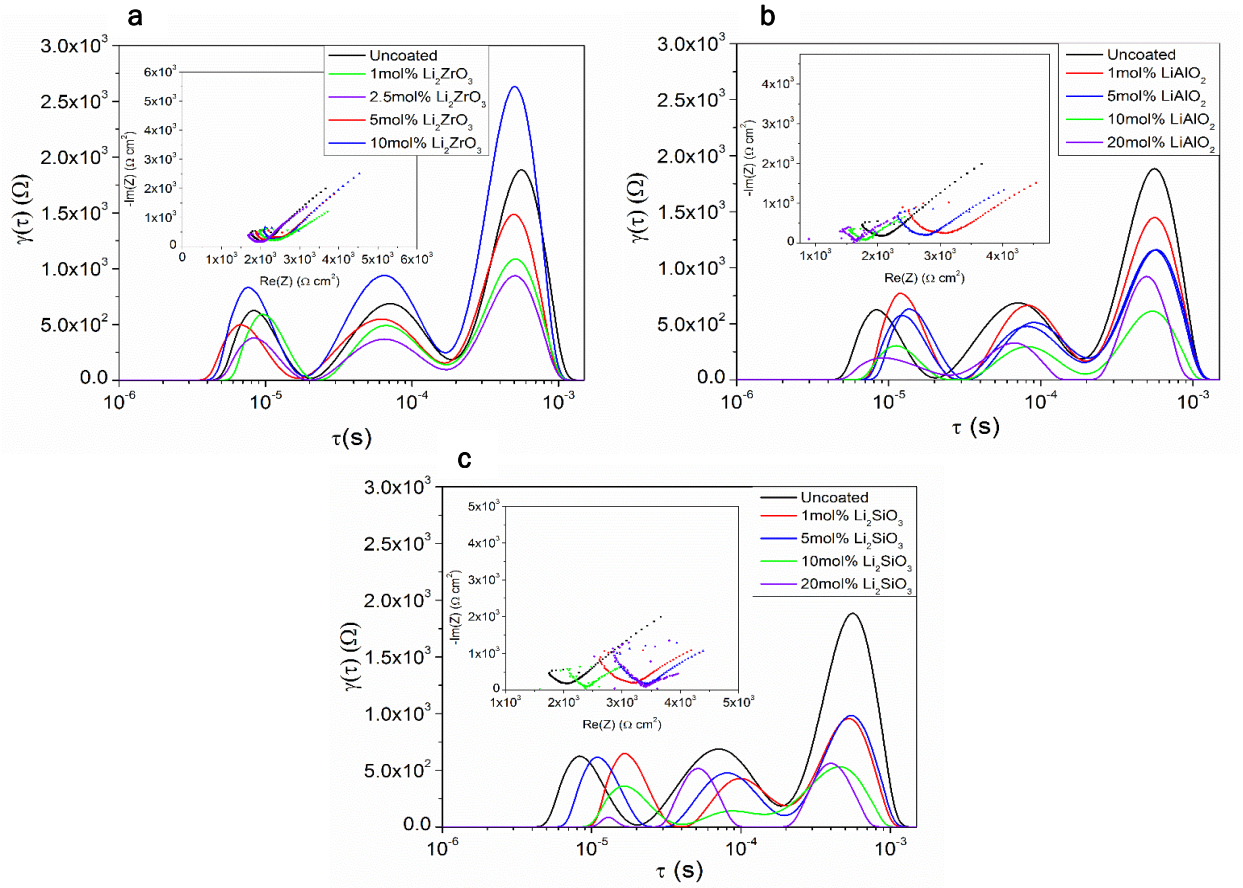

Figure 15. Nyquist plots and Distribution of Relaxation Times Analysis of EIS of a) Li_2ZrO_3-NMC622, b) $LiAlO_2$-NMC622 , and c) Li_2SiO_3-NMC622 co-sintered in a 1:1 wt ratio with LLZTO onto LLZTO trilayers at 1000°C in O_2.

Since the computational results indicated that the Li concentration gradient between NMC and LLZTO is the main driving force for the reaction, more lithiated versions of the silicate and aluminate coatings (Li_5AlO_4 and Li_4SiO_4) were also synthesized and coated on NMC622. These EIS results are shown in Figure 16. At the same molar concentration, the higher lithium content aluminate and silicate reduced the impedance 2x more than their less lithitated counterparts. In addition, 5X reduction in interface resistance was attained for 10mol% excess lithium containing Li_5AlO_4 coated NMC and a 10X reduction in interface resistance was attained with 10mol% of excess lithium for Li_4SiO_4 coated NMC compared to the uncoated samples. This confirms the computational results that reducing the difference in the Li concentration at the interfaces attenuates the interfacial reaction of NMC and LLZTO.

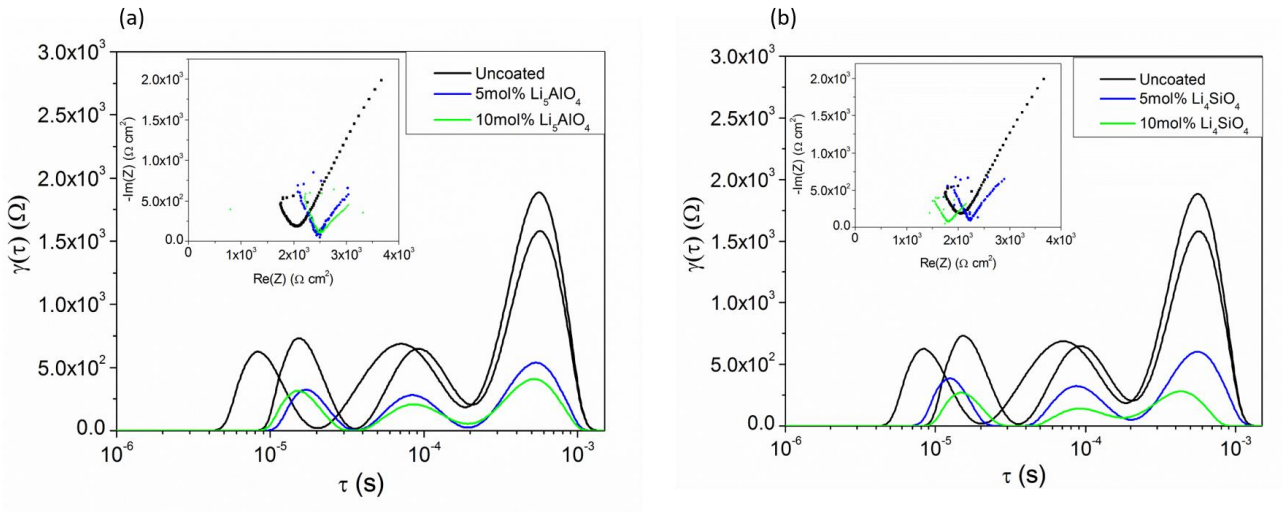

Figure 16. Nyquist plots (inset) and Distribution of Relaxation Times Analysis of EIS of a) Li_5AlO_4-NMC622, and b) Li_4SiO_4-NMC622 co-sintered in a 1:1 wt ratio with LLZTO onto LLZTO trilayers at 1000°C in O_2.

Table 3 summarizes the EIS reduction with various coating materials. From the materials studied Li_4SiO_4 coated NMC with 10mol% excess Li co-sintered sample exhibited 10X reduction in interface resistance compared to the uncoated sample.

Table 3. Comparison on EIS Reduction with Respect to Various Coating Material

Coating	Li_2ZrO_3	Li_3PO_4	$LiAlO_2$	Li_5AlO_4	Li_2SiO_3	Li_4SiO_4
mol%	2.5	10	10	10	10	10
EIS Reduction	2x	1.33X	4x	5x	4x	10x

Trilayer cell with composite NMC-LLZTO cathode layer

As determined by the symmetric cell studies, the lithated aluminate and silicates were identified as prime interfacial coating candidates. These findings were used to develop NMC|LLZTO|Li Metal full cells where the NMC cathode was a mixed composite of 47.5wt% LLZTO, 47.5wt% NMC622, and 5wt% Indium-doped Tin Oxide (ITO). ITO was used as the electronically conductive additive as it was determined O_2 sintering environments were optimal for stabilizing NMC at high temperatures, thus excluding the use of conventional electrically conductive carbon. Despite the shrinkage mismatch between the porous anode tape and the initial formulations of the composite NMC tapes causing extreme curling, full cells were successfully fabricated and infiltrated with Li metal after process optimization. Figure 17 contains an SEM image of a typical NMC622 full

cell before Li metal infiltration, demonstrating the well-sintered contact between the composite cathode and LLZTO separator. The backscatter image shows LLZTO in white, NMC in dark gray, and ITO in light gray.

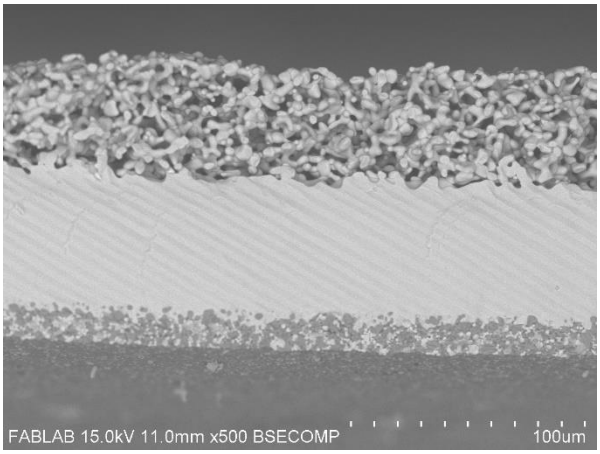

Figure 17. SEM image of a typical full cell displaying a NMC622/LLZTO composite cathode, LLZTO dense layer, and porous LLZTO anode sintered in O_2 at 1050°C.

Figure 18 contains a Nyquist plot of NMC|LLZTO|Li Metal full cells with both Li_4SiO_4 coated NMC622 and uncoated NMC622. Consistent with our symmetric cell studies, the impedance drops by nearly an order of magnitude highlighting the ability of this interfacial coating to improve the interface between LLZTO and NMC622. (Note: This is lower than the interfacial resistance obtained from symmetric cell studies as the sintering temperature here was increased to 1050°C, suggesting that the coating is less effective at reducing the interfacial impedance as the sintering temperature increases past a certain point.). The sintering temperature was increased to ensure complete densification of the dense layer.

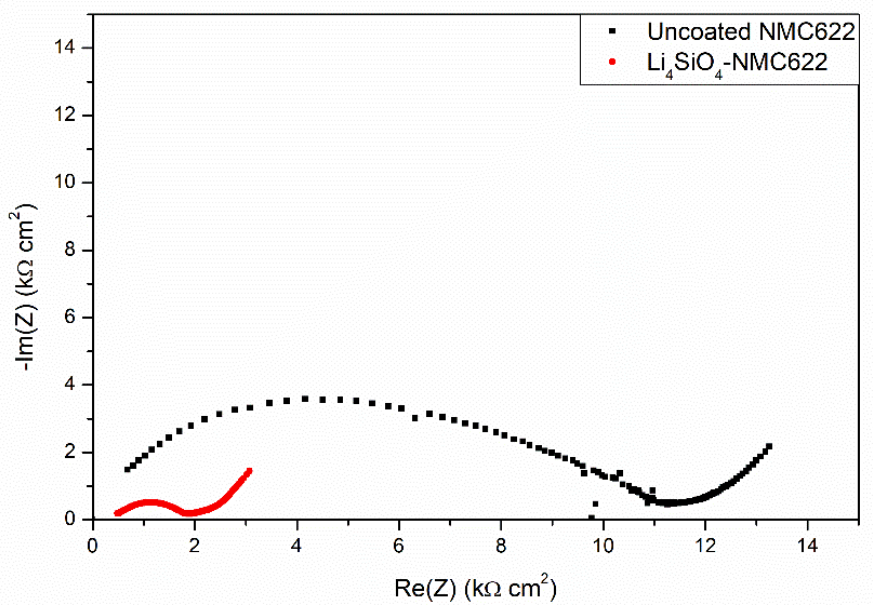

Figure 18. Nyquist of EIS of uncoated and Li_4SiO_4 coated NMC622 Li metal full cells co-sintered in a 1:1 wt ratio with LLZTO onto LLZTO trilayers at 1050°C in O_2.

These cells were then cycled at 60°C at a C/50 charge and discharge rate. The areal loading of these cells was approximately 5.1-5.4mg/cm^2. As demonstrated in Figure 19, both the uncoated and coated NMC622 attain near the theoretical capacity of NMC622 (~200mAh/g) when charged to 4.3V. The voltage drops during charge and discharge were due to equipment errors where cells had to be restarted on the Arbin cycler. It is notable that the charge plateau for Li_4SiO_4-NMC622 is 50-100mV lower than that of the uncoated NMC, suggesting the interfacial coating is beneficial in reducing the overpotential by reducing the degree to which the NMC and LLZTO react and form resistive interphases. Furthermore, the discharge capacity of the cell increases from 75 mAh/g to 94 mAh/g with the introduction of the interfacial coating. This improves the coulombic efficiency (CE) of the cell from 35% to 48%. This is far below the practical discharge capacity of NMC622 (175mAh/g) and usual 1st cycle CEs observed in literature (~80%). While the electrical conductivity of the composite cathode may not be optimal, the low as-assembled ASR suggests that the chemo mechanical volume expansion of NMC may be the cause for the low discharge capacities observed despite the full charge.

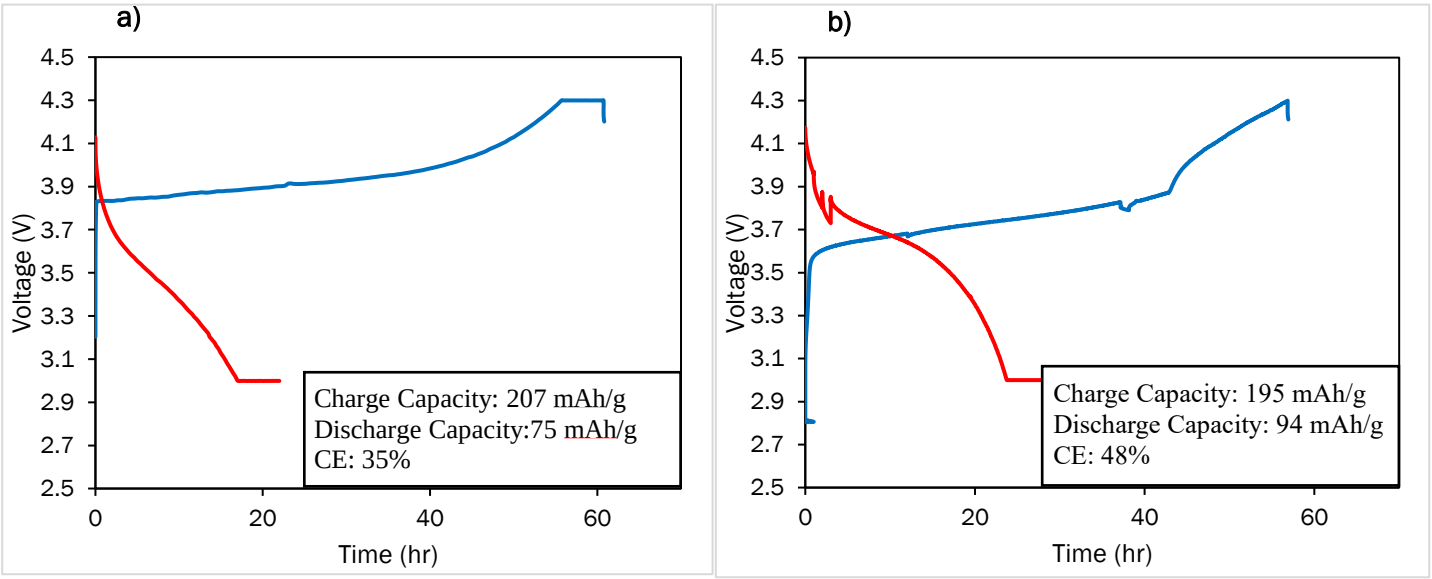

Figure 19. 1st Cycle voltage profiles of a) uncoated NMC622 and b) Li_4SiO_4-NMC622 Full Cells cycled at 60°C at a charge/discharge rate of C/50.

Figure 20 contains the discharge capacity vs cycle number data for the first 5 cycles at a C/50 charge/discharge rate. While the Li_4SiO_4 coating shows improved discharge capacities, it decays to a similar amount of capacity as with the uncoated NMC cells after 5 cycles. This could be due to delamination between the NMC and LLZTO particles caused by the chemo-mechanical expansion of NMC during lithiation/de-lithiation. The cells may still not be achieving the theoretical discharge capacity of NMC622 even on the 1st cycle because of this delamination or because of insufficient electronic conductivity in the composite cathode as this was not within the immediate scope of this project.

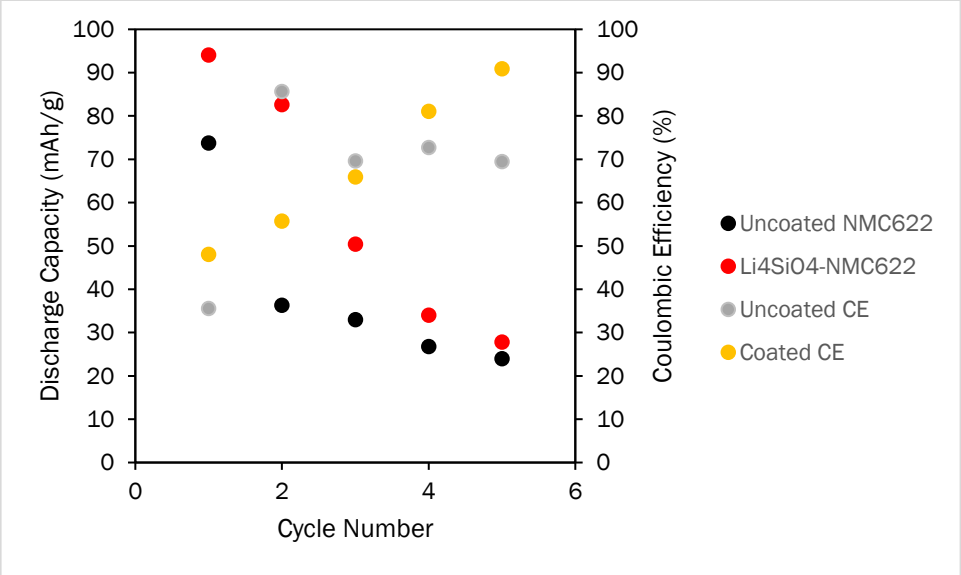

Figure 20. Discharge Capacity and Coulombic Efficiency (CE) vs Cycle number plot for uncoated NMC622 and Li_4SiO_4-NMC622 full cells.

Figure 21 contains the discharge capacy vs cycle number data for high and low Li content aluminate and silicated interfacial coatings. While full cells of each class of coatings improve the discharge capacities of the initial cycles, they quickly decay to less than 30 mAh/g after the 4th or 5th cycle. It should be noted that the initial discharge capacities of the higher Li containing silicate and aluminate are generally greater than those of the lower Li content coatings. While the aluminates have similar discharge capacities, Li_2SiO_3 coated NMC622 only achieves approximately 50mAh/g on the first cycle while the Li_4SiO_4 coating achieves approximately 90 mAh/g. Thus, the Li_4SiO_4 coated NMC622 is the most effective in reducing the interfacial ASR. It is likely that the fast capacity decay is due to the delamination between electrode particles caused by the chemomechanical expansion/contraction of NMC622 particles during cycling. This point if further investigated by performing EIS at the end of charge and discharge.

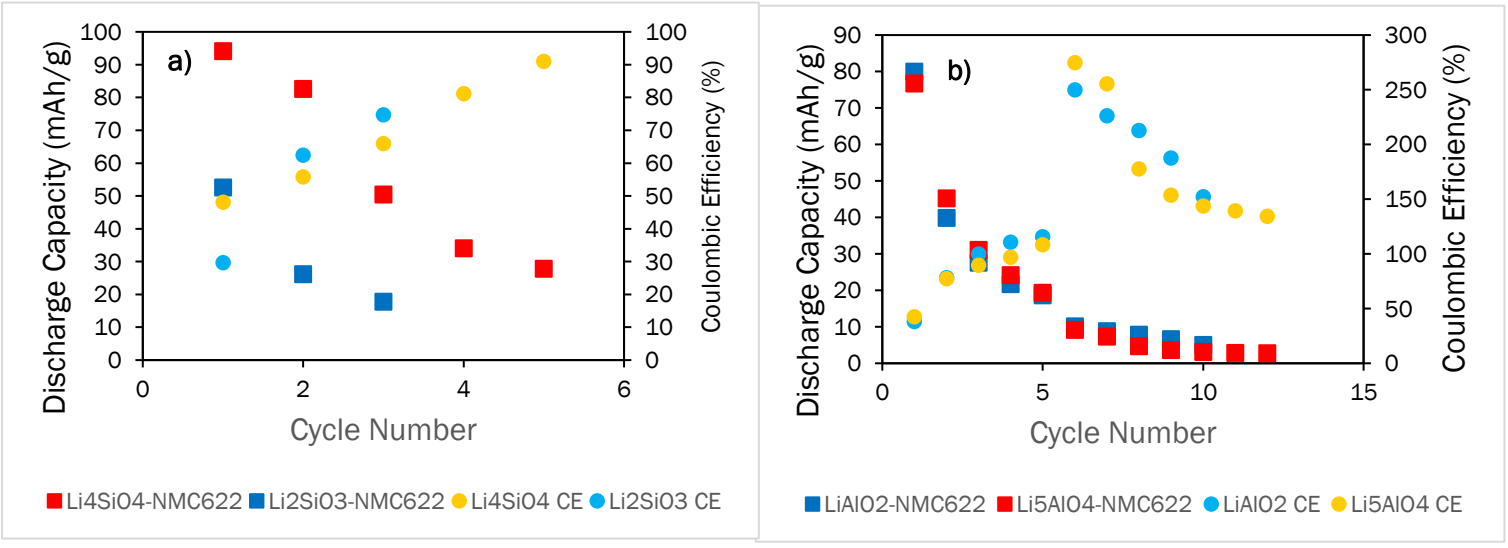

Figure 21. Discharge Capacity and Coulombic Efficiency (CE) vs Cycle number plot for a) silicate-coated NMC622 and b) aluminate-NMC622 full cells.

Figure 22 contains Nyquist plots of EIS taken at the end of charge and discharge. The area-specific resistance (ASR) at the end of charge increases by 50% after the 1st charge and then increases further and stabilizes to approximately 4500 Ω cm^2 after the 2nd cycle. The end of discharge ASR increases steadily after each cycle by 500-1000 Ω cm^2, resulting in a 3x increase compared to the as-assembled case. This growth in ASR is largely observed in the middle frequency region semicircles corresponding to interface phenomena, thus suggesting that the chemo mechanical delamination or electrochemical reactions between electrode particles are the main impediments to stable cycling performance. These will be further explored using SEM and XRD respectively. The greatest increase in ASR occurs during the charge step of the 1st and 2nd cycles initially since the end of charge ASR stabilizes after the 2nd cycle, indicating that an in-depth understanding of the ASR growth during charge is needed. To investigate further, another experiment was performed that measured the ASR using EIS every 100mV during the charge step.

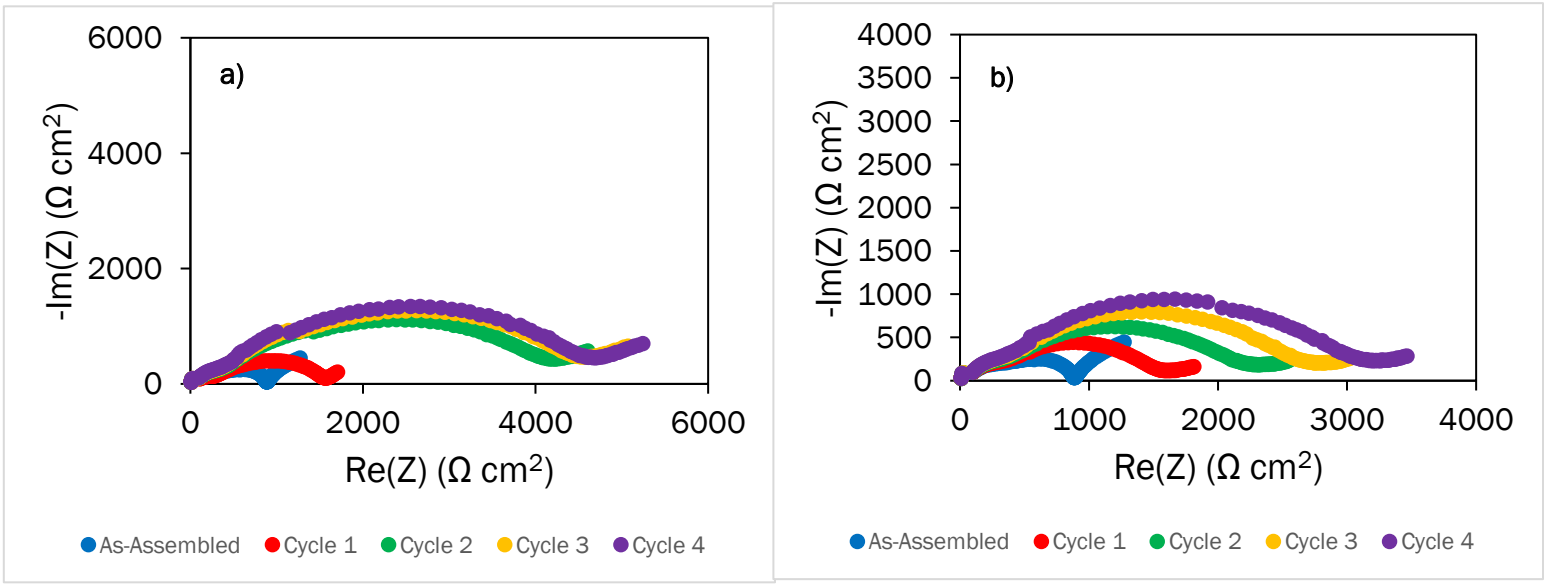

Figure 22. Nyquist plots of Li_4SiO_4-NMC622 full cells at a) the end of charge and b) at the end of discharge.

Conclusions

The reactivity of NMC with LLZTO increases with increasing Ni content. The reaction is mainly caused by Li deficiency at high temperature. Apart from optimum Li content effect of sintering atmosphere was also studied. O_2 atmosphere is suitable for the co-sintering studies of NMC with LLZTO as it suppresses the loss of O_2 that NMC experiences at elevated temperatures, thereby reducing the structural degradation and formation of resistive interphases. Furthermore, interface coated NMC using the optimum amount of excess Li can suppress the formation of the perovskite phase. First-principles computation was used to study the trends in stability with LLZO and NMC through varying Li and O_2 chemical potential. EIS measurements on NMC/trilayers and LLZTO/NMC symmetric cells found that Li_4SiO_4 is better than any other interface coating material at improving the interfacial impedance.(10x reduction). Moreover, increasing the amount of available Li during co-sintering can dramatically reduce the reaction of NMC and LLZTO achieving a 10X reduction in interfacial area-specific resistance (ASR). Studies on all-solid-state full cells were conducted and the Li_4SiO_4 interface coating reduced the overall impedance by nearly an order of magnitude compared to the cell with no interfacial coating. Full cell cycling results further supported the efficacy of the Li_4SiO_4 coating in improving the discharge capacity. However, capacity fade on subsequent cycles is quite severe. EIS results of the full cells at the end of charge and discharge demonstrated a large ASR growth after the first several cycles which explains the fast discharge capacity decay. This decay is likely due to the delamination between NMC and LLZTO particles that occurs because of the chemo-mechanical volume changes that NMC undergoes during lithiation/de-lithiation. Additionally, the electrical conductivity of the cathode composite is likely low despite the addition of ITO as a

conductive additive. Further studies should focus on improving the electronic conductivity of the composite cathode in addition to methods of alleviating the chemo-mechanical delamination between NMC and solid electrolyte particles during cycling.

Key Publications

Patent

Yaoyu Ren & Eric D. Wachsman, "Interlayer for Solid Cathode-Electrolyte Interface," Invention Disclosure

Papers

"Solid-State Chemistries Stable with High-Energy Cathodes for Lithium-Ion Batteries", A.M. Nolan, Y. Liu, Y. Mo, *ACS Energy Letters*, **4**, 2444-2451 (2019)

"Li+ Diffusion in Amorphous and Crystalline Al2O3 for Battery Electrode Coatings", A.M. Nolan, D. Wickramaratne, N. Bernstein, Y. Mo, M. D. Johannes, *Chemistry of Materials* **33**, 19, 7795–7804 (2021)

"Interfacial Defect of Lithium Metal in Solid-State Batteries", M. Yang, Y. Mo, *Angewandte Chemie* **60**, 21494, (2021)

"Interfacial Atomistic Mechanisms of Lithium Metal Stripping and Plating in Solid-State Batteries", M. Yang, Y. Liu, A.M. Nolan, Y. Mo, *Advanced Materials* **33,** 2008081 (2021)

"Computation-Guided Discovery of Coating Materials to Stabilize the Interface Between Lithium Garnet Solid Electrolyte and High-Energy Cathodes," A. M. Nolan, E. D. Wachsman & Y. Mo, *Energy Storage Materials*, **41**, 571-580, (2021)

"Effect of the 3D Structure and Grain Boundaries on Lithium Transport in Garnet Solid Electrolytes," A. Neumann, T. R. Hamann, T. Danner, S. Hein, K. Becker-Steinberger, E. D. Wachsman, and A. Latz, *Applied Energy Materials*, (2021)

"Challenges for and Pathways toward Li-Metal-Based All-Solid-State Batteries,", P. Albertus, V. Anandan, C. Ban, N. Balsara, I. Belharouak, J. Buettner-Garrett, Z. Chen, C. Daniel, M. Doeff, N.J. Dudney, B. Dunn, S.J. Harris, S. Herle, E. Herbert, S. Kalnaus, J.A. Libera, J. Nanda, J. Sakamoto, E.C. Self, S. Tepavcevic, E.D. Wachsman, C. Wang, A.S. Westover, J. Xiao, and T. Yersak, *ACS Energy Letters*, **6**, 1399-1404 (2021).

"All Solid-State Li/LLZO/LCO Battery Enabled by Alumina Interfacial Coating," Y. Ren and E.D. Wachsman, *Journal of The Electrochemical Society*, **169**, 040529 (2022).

"Oxide-Based Solid-State Batteries: A Perspective on Composite Cathode Architecture," Y. Ren, T. Danner, A. Moy, M. Finsterbusch, T. Hamann, J. Dippell, T. Fuchs, M. Müller, R. Hoft, A. Weber, L.A. Curtiss, P. Zapol, M. Klenk, A.T. Ngo, P. Barai, B. Wood, R. Shi, S. Wan, T. Wook, M. Engels, J. Nanda, F. Richter, A. Latz, V. Srinivasan, J. Janek, J. Sakamoto, D. Fattakhova-Rohlfing, and E.D. Wachsman, *Advanced Energy Materials*, 2201939 (2022) **– *Editor's Choice***

Menghao Yang, Yunsheng Liu, Yifei Mo*, "Lithium Crystallization at Solid Interfaces", Nature Communications, 14, 2986 (2023)

Presentations

E.D. Wachsman, "Enabling High-Rate Lithium Metal Anodes by Tailored Structures and Interfaces", Materials Research Society, April 2023, San Francisco, CA - ***Invited***

R.M. Hoft, E.D. Wachsman, “Enabling the High-Temperature Co-Sintering of NMC and Li-Stuffed Garnets”, The Electrochemical Society, May 2023, Boston, MA

E.D. Wachsman, “Enabling High Rate Metal Anodes by Tailored Structures and Interfaces”, International Conference on Solid State Ionics, July 2022, Boston, MA**– *Keynote***

Y. Mo, “Data-Driven Discovery of Materials for Next-Generation Batteries”, “Frontiers in Computational Materials Science”, UW-Madison Computation In Engineering Forum 2022 (10/2022) - ***Invited***

Y. Mo, “Computation Guided Design of Materials for Solid-State Batteries”, Department of Chemical Engineering, Columbia University (10/2022) - ***Invited***

Y.Mo, “Understanding and Rational Design of Disordering in Super-Ionic Conductors by First Principles Computation and Machine Learning”, MRS meeting, San Francisco, CA (04/2023) ***- Invited***

E.D. Wachsman, “Enabling High Rate Metal Anodes by Tailored Structures and Interfaces,” Lithium Metal Anodes and their Application in Batteries, February 2022, Webinar ***- Keynote***

Y. Mo, “Interfacial Failure of Lithium Metal in Solid-State Batteries: Insight from Large-Scale Atomistic Modeling”, Beyond Lithium Ion XIII, Argonne National Laboratory (virtual) June 2021 ***- Invited***

Y. Mo, “Computation Accelerated Design of Materials and Interfaces for Solid-State Batteries”, Phonon Science Seminar, SLAC (virtual) May 2021 ***- Invited***

A. Nolan, Y. Mo, “Computation-Guided Discovery of Materials for Stabilizing Interfaces in High-Energy Solid-State Lithium-Ion Batteries”, MRS Spring Meeting, Seattle WA April 2021

Y. Mo, “Interfacial Atomistic Mechanisms of Lithium Metal Stripping and Plating in Solid-State Batteries”, The 10th International Conference on Multiscale Materials Modeling (MMM10), Baltimore MD (10/2022)

Y. Mo, “Data-Driven Discovery of Materials for Next-Generation Batteries”, “Frontiers in Computational Materials Science”, UW-Madison Computation In Engineering Forum 2022 (10/2022) ***- Invited***

Y. Mo, “Computation Guided Design of Materials for Solid-State Batteries”, Department of Chemical Engineering, Columbia University (10/2022) ***- Invited***

Y. Mo, “Interfacial Failure of Lithium Metal in Solid-State Batteries: Insight from Large-Scale Atomistic Modeling”, Beyond Lithium Ion XIII, Argonne National Lab (06/2021) ***- Invited***

E.D. Wachsman, “A Solid Transformation of Energy Storage,” Materials Research Society, December 2021, Boston ***- Invited***

E.D. Wachsman, “A Solid Transformation of Energy Storage,” World Conference on Solid Electrolytes, October 2021 ***- Invited***

E.D. Wachsman, “A Solid Transformation of Energy Storage,” Iowa State University, MSE Seminar, February 2021 ***- Invited***

A. Nolan, Y. Liu, Y. Mo, “Solid-State Chemistries Stable with High-Energy Cathodes for Lithium-Ion Batteries”, ECS PRIME (10/2020) ***- Invited***

Y. Mo, “Data-Driven Discovery of New Materials for Solid-State Batteries”, ECS PRIME (10/2020) • E.D. Wachsman, “A Solid Transformation of Energy Storage,” NDIA, Military Power Sources Committee, December 2020 ***- Invited***

E.D. Wachsman, “A Solid Transformation of Energy Storage,” StorageX, Stanford University, November 2020 ***- Keynote***

E.D. Wachsman, “Beyond Dendrites, Cycling Li-Metal Across Garnet at High Current Densities,” AABC, November 2020 ***- Invited***

E.D. Wachsman, “Ultra-Safe, High-Energy-Density, Solid-State Batteries for Extreme Temperatures,” 2020 Conference on Advanced Power Systems for Deep Space Exploration, October 2020 ***- Invited***

E.D. Wachsman, “Safe, High-Energy-Density, Solid-State Batteries,” Battery Systems Panel, AIEE/IEEE Electric Aircraft Technologies Symposium, August 2020 ***- Invited***

E.D. Wachsman, “Safe, High-Energy-Density, Solid-State Li Batteries,” Frontiers for Next Generation Lithium Batteries, American Ceramic Society, July 2020 ***- Invited***

E.D. Wachsman, “Beyond Dendrites, Cycling Li-Metal Across Garnet at High Current Densities,” Electrochemical Society Meeting, October 2019, Atlanta, GA ***- Invited***

References

[1] A.M. Nolan, Y. Zhu, X. He, Q. Bai, Y. Mo, “Computation-Accelerated Design of Materials and Interfaces for All-Solid-State Lithium-Ion Batteries”, Joule, 2, 2016-2046 (2018)

[2] X. He, Y. Zhu, Y. Mo, “Origin of Fast Ion Diffusion in Super-Ionic Conductors”, Nature Communications, 8, 15893 (2017)

[3] X. Han, Y. Gong, X. He, G.T. Hitz, J. Dai, Y. Mo, V. Thangadurai, E.D. Wachsman, L. Hu “Negating Interfacial Impedance in Garnet-Based Solid-State Li-Metal Batteries”, Nature Materials, 16, 572 (2017)

[4] W. Luo, Y. Gong, Y. Zhu, K. Fu, J. Dai, S. Lacey, C. Wang, B. Liu, X. Han, Y. Mo, E.D. Wachsman, L. Hu “Transition from Super-lithiophobicity to Super-lithiophilicity of Garnet Solid-State Electrolyte”, Journal of the American Chemical Society, 138, 12258-12262 (2016)

Acknowledgements

We greatly thank Office of Energy Efficiency & Renewable Energy, Department of Energy for funding this project, without which we could not have achieved the significant progress detailed in this report.